Journal of Physics and Chemistry of Solids 118 (2018) 6–13

Contents lists available at ScienceDirect

Journal of Physics and Chemistry of Solids

journal homepage: www.elsevier.com/locate/jpcs

Structure, thermal, and impedance study of a new organic–inorganic hybrid $[(CH_2)_7(NH_3)_2]CoCl_4$

M.F. Mostafa *, Sh. S. El-khiyami, S.K. Alal [1]

Physics Department, Faculty of Science, University of Cairo, Giza, Egypt

ARTICLE INFO

Keywords:
Conductivity
Dielectric constant
Phase transition
X-ray crystal structure

ABSTRACT

$[(CH_2)_7(NH_3)_2]CoCl_4$ crystallizes in the triclinic system, space group P-1 with two molecules per asymmetric unit cell ($Z = 2$). The unit cell dimensions are $a = 7.3107$ (2) Å, $b = 10.1841$ (3) Å, $c = 11.2690$ (4) Å, $\alpha = 66.81$ (2), $\beta = 78.85$ (12), and $\gamma = 87.66$ (2). The unit cell volume and the calculated density are 756.11 (4) $Å^3$ and 1.463 Mg m^{-3}, respectively. The structure of the hybrid is characterized by alternating layers of inorganic $[CoCl_4]^{2-}$ anion and heptane diammonium cation. The organic hydrocarbon layers are packed in a stacked herring-bone manner with hydrogen bonds to the halide ions. The lattice potential energy U_{pot} and the cation molecular volume V^+ are 1856.2 kJ/mol and 0.37 nm^3, respectively. DSC showed a compound (broad) peak at $T_1 = 331$ K, $T_2 = 328$ K with total entropy $\Delta S = 36.2$ J/K. mol, and a λ-like endothermic peak at $T_3 = 296$ K ($\Delta S = 24.9$ J/K. mol). Dielectric properties are investigated at different temperatures and frequencies [260 K < T < 360 K and 0.06 kHz < f < 60 kHz, respectively]. Super-linear power law is observed for the AC conductivity, which is analyzed based on the jump relaxation model.

1. Introduction

In recent years, the synthesis, structure, thermal, and physicochemical properties of organic–inorganic hybrids (OIHs) have attracted significant attention due to their practical applications in solar cell and optoelectronics [1–4] as well as their unique fundamental scientific prospects concerning low-dimensional magnetic interactions and their intriguing thermal dielectric and ferroelectric properties [5–7]. OIHs provide the basis for developing systems that combine bilayer characteristics within a crystalline lattice. The series of A_2MX_4, where A is an alkyl monoammonium or alkylene diammonium ion, M a divalent metal ion, and X a halide ion, are excellent models to study OIH properties. Variations in A, M, and X provide an excellent opportunity to tailor the material to adjust its physical and chemical properties for industrial purposes. Besides, long-chain hybrids are of special interest as they show several consecutive phase transitions and are good models of lipid membranes [8,9]. Being solids, they provide a means to study properties of biological membranes by solid-state techniques. Crystal structure analysis of short- and long-chain diprotonated hybrids $[(CH_3)_n(NH_3)_2]MX_4$, where X = Cl/Br, was performed for a few members of this series. This revealed that the structure of M = Mn, Fe [10], Cu [11], and Cd [12–14] is monoclinic with $P2_1/c$ or $P2_1/n$ for an even number of C atoms and orthorhombic for an odd number of C atoms in hybrids where n = 2-5 [15]. These hybrids form layers of associated $[MCl_6]$ octahedra extending in a two-dimensional network, which are different from those with M = Co (n = 3 and 5) and Zn (n = 3), which crystallize in the monoclinic system with $P2_1/n$ or $P2_1/c$ and form layers of unassociated tetrahedrally distorted $[CoCl_4]$ and $[ZnCl_4]$, respectively [16–18]. As the chain length increases (n > 5), all Co and Zn hybrids (n = 6-10) crystallize in the triclinic system sp. gr P-1 [19–25]. Thus it is clear that the room temperature structure of short-chain hybrids with n = 2-5 is different from that of intermediate- and long-chain ones (n = 6, …, 10), where short-chain hybrids' crystal symmetry alternates between monoclinic and orthorhombic forms depending on the parity, whereas all hybrids with $6 \leq n \leq 10$ are triclinic P-1.

A previous study by our group of the thermal, dielectric, and con-

* Corresponding author.
E-mail address: Mohga40@Yahoo.com (M.F. Mostafa).
[1] In partial fulfillment of the Ph.D. degree.

https://doi.org/10.1016/j.jpcs.2018.02.048
Received 1 July 2017; Received in revised form 19 February 2018; Accepted 20 February 2018
Available online 23 February 2018

ductivity properties of n = 3 and M = Cu [26]; n = 6 and M = Fe, Co, or Zn [20,21,27]; n = 7 and M = Co [22,23]; n = 9 and M = Cu [28]; n = 10 and M = Cd [29]; n = 12 and M = Co, Cu, or Cd [30–32] showed phase transitions between 150 K and 420 K. The number and type of the transitions depend on both the chain length and the metal ion. Some of these hybrids showed commensurate to incommensurate structure changes [31]. Tetrahedrally coordinated $[CoCl_4]$ hybrids have been of interest mainly due to their magnetic properties [33–35]. A recent study of $[(CH_2)_7(NH_3)_2]CoCl_{4-x}Br_x$, where x = 2 and 4, referred to as 7CoCB and 7CoB, respectively, showed that the structure consists of infinite two-dimensional sheets of tetrahedrally coordinated $[CoCl_2Br_2]/[CoB_4]$ anions parallel to the *ac* plane [22,23]. The anion sheets are separated by the layered cation chains. The structure is stabilized through the interaction of the two sheets via N-H ···· X bonding. The bromide hybrid shows discontinuous phase transition associated with an abrupt change from insulator to semiconductor at T = 343 K [23]. To investigate the effect of halide ion on the phase change and conductivity behavior as well as on the chain length effect, we prepared and characterized the corresponding chloride, namely $[(CH_2)_7(NH_3)_2]CoCl_4$, referred to as 7CoC. Crystal structure analysis and thermal, dielectric, and conductivity measurements were performed at temperatures between 260 K and 360 K and at frequencies between 60 Hz and 60 kHz.

2. Experimental

7CoC was prepared by mixing an alcoholic solution of 1,7-diammonium-dichloroheptane and the corresponding metal chloride in a 1:1 ratio. The solution was heated at 70 °C for 1 h. Small crystallites precipitated out upon gradual cooling to room temperature. The crystallites were filtered, washed, and recrystallized twice from the alcoholic solution. Single crystals were grown from ethanol kept in a desiccator for one month at room temperature.

Chemical analysis was performed at the Micro Analysis Center at the University of Cairo. The results of this analysis gave the following measurements: percent of carbon = 24.81% (25.248) and hydrogen = 5.86% (6.053%) for 7CoC, with the theoretical values given in brackets. These results indicated differences within experimental error, thereby confirming the formation of the desired compound.

The IR spectrum was obtained using an FTIR 1650 Perkin Elmer spectrometer. The IR spectrum and chemical analysis results confirmed the formation of the sample with chemical formula $[(CH_2)_7(NH_3)_2]CoCl_4$.

Differential thermal scanning (DSC) measurements were performed on a Shimadzu thermal scanner model DSC-50 at 5 °C/min. Powdered crystals weighing 2.5 mg were used. Measurements were performed under a flow of dry nitrogen gas at a rate of 50 ml/min. Data were calibrated using the melting transition of indium at 157 °C.

X-ray crystallographic data were collected on an Enraf-Nonius 590 Kappa CCD single crystal diffractometer with graphite monochromator using MoKα (λ = 0.71073 Å). Intensities were collected at room temperature using the φ-ω-scan mode. Unit cell refinement and data reduction were performed using Denzo and ScalePak programs [36].

The crystal structure was solved by the direct method using the SIR92 program [37], which revealed the positions of all non-hydrogen atoms, and refined by the full matrix least-square refinement based on F^2 using the maXus package [38]. The temperature factors of all non-hydrogen atoms were refined anisotropically, and then hydrogen atoms were introduced as a riding model with C-H = 0.96 and refined isotropically. Molecular graphics were prepared using the ORTEP program [39].

Complex dielectric constant ε* was measured using a computer-controlled lock-in amplifier-type EG&G model 5207. Samples are 1 cm in diameter and 1.2 mm thick. Surfaces were coated with silver paste to ensure good electrical contact. A home-built cryostat was used for measurements between liquid nitrogen temperature and 425 K. Temperature was measured using a copper–constantan thermocouple. The sample chamber was flushed several times with dry nitrogen gas and evacuated for 24 h before starting measurements.

3. Results and discussion

3.1. Crystal structure

Fig. 1a and 1 b show the ORTEP view of the molecules and molecular arrangement in the unit cell. The H-bond network along the "*a*" direction is shown in Fig. 1c Fig. 1d shows the arrangement of $[CoCl_4]^{2-}$ tetrahedra in the "*b*" direction. Table 1 lists data collection parameters of 7CoC. Table 2 lists fractional atomic coordinates and equivalent isotropic thermal parameters. Anisotropic displacement parameters are listed in Table 3. Selected bond length (Å) and bond angles (°) are shown in Table 4. All structure information can be obtained from the Cambridge Crystallographic Data Center (Deposit Number CCDC-1570160) [40]. The crystal structure of 7CoC consists of two isolated cations and tetrahedrally distorted metal halide $[CoCl_4]^{2-}$ anions. The anions alternate with layers of diammonium cations. Both anions and cations are related by a center of inversion. Cation chains are hydrogen bonded to Co–halide tetrahedra. The average Co–Cl bond length is 2.276 Å, the largest difference in bond lengths is 0.046 Å, and the largest difference in Cl–Co–Cl bond angles is ~4°, compared with perfect tetrahedra. $[(CH_2)_7(NH_3)_2]^{2+}$ cations have a zigzag chain structure with an average bond length of 1.51 Å for C–N. These results are in good agreement with the bond length of other diammonium hybrids studied previously [16,18,22,41].

The chains are completely isolated from each other as there are no contacts shorter than 3.0 Å between neighboring chains and enough space between chains makes their large thermal vibrations physically reasonable. The C atoms of the cations show large thermal displacement compared with those of the anions, which suggests disorder. Table 4 indicates that the chains have nearly an all-*trans* conformation on one end; at the terminal N14, the dihedral angle (C10–C11–C12–N14) = –173.4° (12). The other end of the chain is disordered, particularly in the area near the terminal ammonium group, where a gauche conformation has a dihedral angle (C8–C7–C6–N13) = 66.7° (10). This optimizes the packing density of the organic chains. The organic cations and inorganic anions are hydrogen bonded. Anions form unassociated pseudo-infinite two-dimensional sheets parallel to the *ac* plane. Alkyl chains act as spacers between these sheets. Adjacent layers are pillared by the alkyl chains of the organic cations.

3.2. Lattice potential energy, molecular volume, and cation volume

An estimation of the lattice potential energy (U_{pot}) for samples with molecular formula M_pX_q (where p = q = 1), such as the currently studied hybrids, is obtained using Eqs. (1)–(3)

$$U(pot) = \Sigma\, n_i z^2\, [\, \alpha/V^{1/3} + \beta] \quad (1)$$

where α and β are appropriate fitting coefficients chosen according to the stoichiometry of the hybrid, n_i is the number of ions with a charge z_i in the formula unit, and V_m is the molecular volume.

For MX_2 (1:2) hybrids, the lattice potential energy is given by [42].

$$U(pot) = |\, Z^+||Z^-|\nu\, [\alpha/V^{1/3} + \beta] \quad (2)$$

where Z^+ and Z^- are the respective charges on the cation and anion of the compound, respectively, ν is the number of ions per molecule and equals to $(p + q)$. For the case of hybrids of formula MX_2 with charge ratio (1:2) $Z^+ = 2$, $Z^- = 1$, p = 1, q = 2, $\nu = 3$, $\alpha = 133.5$ kJ mol^{-1} nm, and $\beta = 60.9$ kJ mol^{-1}, V_m (nm^3) is given by [42]:

$$V_m\ (nm^3) = M_m/(\rho N_A) = 1.66045 \times 10^{-3} M_m/\rho \quad (3)$$

where N_A is Avogadro's number, ρ (g.cm^{-3}) is the density, and M_m (g/mol) is the molar mass as obtained from the crystal structure information listed in Table 1. For the presently investigated hybrids, MX (1:1), with

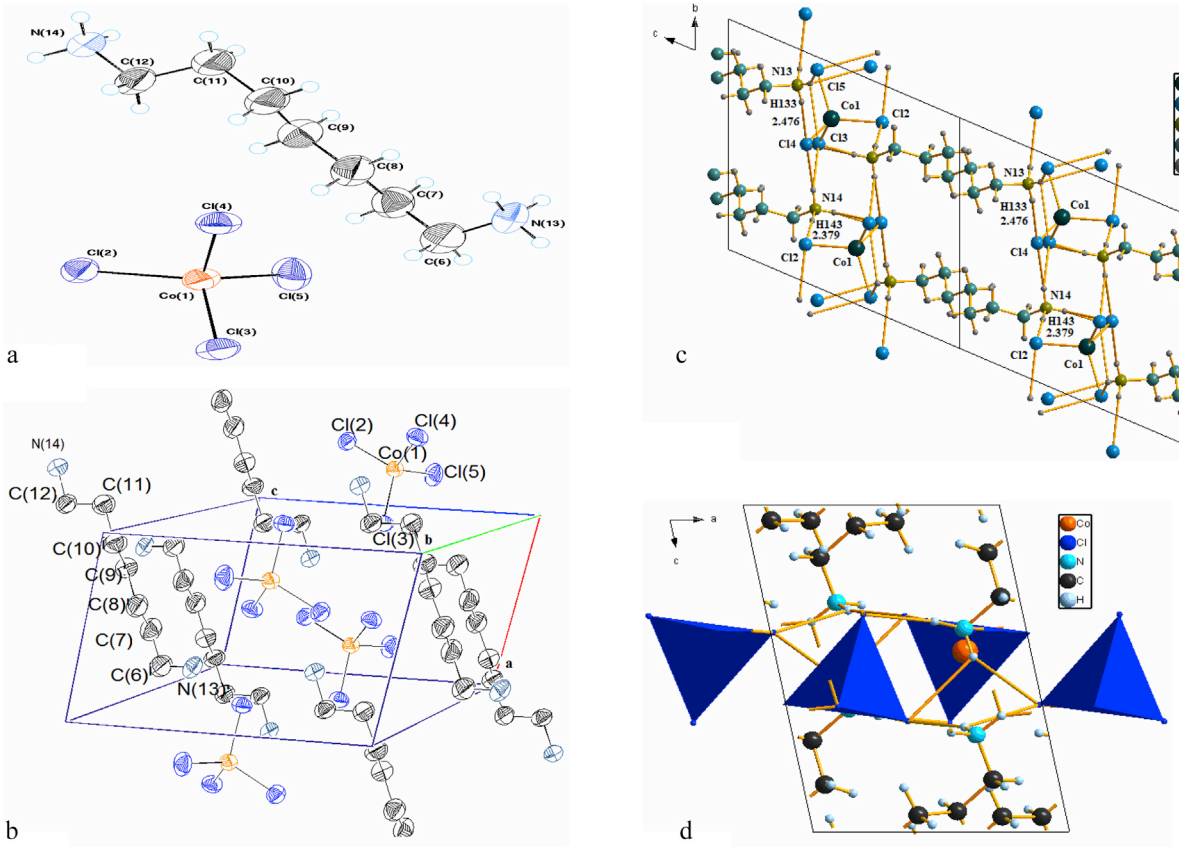

Fig. 1. a: ORTEP view of the atoms in molecule.
Fig. 1. b: ORTEP view of molecular arrangement in unit cell.
Fig. 1. c: H-bond network in the a direction (red dotted line).
Fig. 1. d: Arrangement of [CoCl4]2– tetrahedra along the b direction.

charge ratio (2:2), $z+ = 2$, $z- = 2$, $p = 1$, $q = 1$, $\nu = 2$, $\alpha = 117.3$ kJ mol^{-1} nm, and $\beta = 51.9$ kJ mol^{-1}; V_m is presented in units of nm^3 [42,43]. Using Eq. (3), the calculated V_m is 0.37 nm^3 for 7CoC. This yields lattice energy $U_{pot} = 1856.2$ kJ/mol. The volume of the cation (V^+) and anion (V^-) for materials with chemical formula M_pX_q is given by Eq. (4) [43].

$$V_m = pV^+ + qV^- \quad (4)$$

Using Eq. (4) where for MX (1:1), $p = 1$ and $q = 1$, and anion volume of $[CoCl_4]^{2-} = 0.196$ nm^3 [43], V^+ (the volume of the cation $[C_7H_{20}N_2]^{2+}$) becomes 0.182 nm^3. The lattice potential energy and molecular volume of Co organic–inorganic hybrids $[(CH_2)_n(NH_3)_2]CoCl_4$ (n = 3, 5, and 6) as well as those of $[(CH_2)_7(NH_3)_2]CoCl_2Br_2$ and $[(CH_2)_7(NH_3)_2]CoBr_4$ were calculated using previously published X-ray structure results. Table 5 lists the calculated (U_{pot}) (kJ/mol), (V_m) (nm^3), and cation volume (V^+) (nm^3) of chloride hybrids for comparison. It is clear that as chain length increases, the molecular volume increases and lattice potential energy decreases. The effect of halide ion replacement results in a decrease of lattice potential energy as bromide ion replaces chloride, indicating decrease of the binding energy with increase of bromide ion.

3.3. Thermal behavior: differential thermal scanning (DSC) of 7CoC

The DSC thermograph of 7CoC, measured on heating at temperatures between 260 K and 410 K, is depicted in Fig. 2a Thermal parameters are listed in Table 6. Starting from the high temperature side, a very broad endothermic transition between 324 K and 334 K most likely corresponds to two transitions at $T_1 = 331 \pm 2$ K and $T_2 = 328 \pm 1$ K. Calculation of the entropy change of the broad peak is found to be $\Delta S = 36.2$ J/K. mol. Such a large entropy value is usually associated with order–disorder phase change attributed to rotation and/or conformations of the organic chain [6,30,44–48]. Another λ-like transition appears at $T_3 = 296 \pm 2$ K with onset temperature of 282 K and entropy change $\Delta S = 24.9$ J/K. mol. The shape and entropy values imply a first-order phase change. As a further confirmation of the structure transition, X-ray powder diffraction measurements were performed using a Siemens (D5000) diffractometer (Ni-filtered Cu-K radiation) of wave length $\lambda = 1.54057$ Å. A film of uniform thickness was used. Scans were recorded at every 0.05 step between $2\theta = 10$ and 90° at T = 295 K, 320 K, 350 K, and 430 K. Diffraction patterns at the specified temperatures are shown in Fig. 2b. The graph shows structural changes such that the sample remains in the crystalline phase up to 350 K. It collapses at T = 430 K.

3.4. Dielectric constant

3.4.1. i Temperature dependence of the dielectric constant

To study phase transitions of this hybrid, temperature and frequency dependence were evaluated at temperatures between 260 K and 360 K. The real part (ε′) of complex dielectric constant in the temperature range 260 K < T < 360 K measured on heating is shown in Fig. 3a. Above room temperature, the dielectric constant (ε′) shows a peak with two maxima at $T_2 = 328$ K and $T_1 = 331$ K in the low-frequency range, which merge into a single peak at high frequency. The temperature of the peak is frequency dependent. It is clear that values of ε′ decrease with increasing frequency and are not annihilated at the highest measured frequency (f = 60 kHz). Dependence of the dielectric constant (ε′) on temperature and frequency reflects the consecutive phase changes observed in the DSC results. Insert (i) of Fig. 3 a shows a small symmetric dielectric

Table 1
X-ray data collection parameters of 7CoC.

	7CoC
Empirical formula	$C_7H_{20}N_2CoCl_4$
M_r	332.996
Space group	Triclinic P1
a	7.3107 (2)Å
b	10.1841 (3)Å
c	11.2690 (4)Å
α	66.810 (2)°
β	78.8588 (12)°
γ	87.664 (2)°
V	756.11 (3)Å^3
Z	2
D_x	1.463 Mg m^{-3}
λ	0.71073
θ_{max}	30.06°
μ	1.81 mm^{-1}
T	298 K
Shape	Cube
color	Blue
measured reflection	4357
independent reflections	4943
observed reflections	1993
Criterion	I > 3.00 sigma(I)
R_{int}	0.037
H	−10 → 10
K	−12 → 14
L	0 → 15
R (all)	0 .1055
R (gt)	0.066
wR (ref)	0.125
wR (all)	0.138
S (ref)	1.551
S (all)	1.198
Δ/σ_{max}	0.044
$\Delta\rho_{max}$	3.45eÅ^3
$\Delta\rho_{min}$	−3.75eÅ^3
wR (gt)	0.125
S (all)	1.19

Table 2
Fractional atomic coordinates and equivalent isotropic thermal parameters $U_{eq} = 1/3\Sigma_i\Sigma_j U_{ij} a_i^* a_j^* \boldsymbol{a}_i \boldsymbol{a}_j$ of 7CoC.

7CoC	X	Y	Z	U_{eq}
Co1	0.7434 (14)	0.2452 (11)	0.4473 (10)	0.050 (6)
Cl2	0.6233 (14)	0.1640 (11)	0.6661 (10)	0.055 (6)
Cl3	1.0126 (14)	0.3749 (11)	0.3896 (10)	0.059 (6)
Cl4	0.5386 (14)	0.3990 (11)	0.3388 (10)	0.061 (6)
Cl5	0.7988 (14)	0.0560 (11)	0.3841 (10)	0.075 (6)
N14	−0.2421 (14)	0.6644 (11)	0.3771 (10)	0.055 (6)
C12	−0.0724 (14)	0.7433 (11)	0.2803 (10)	0.065 (6)
N13	0.7172 (14)	0.8414 (11)	−0.2977 (10)	0.062 (6)
C11	−0.0857 (14)	0.7627 (11)	0.1453 (10)	0.074 (6)
C9	0.2493 (14)	0.7263 (11)	0.0482 (10)	0.084 (6)
C10	0.0968 (14)	0.8278 (11)	0.0471 (10)	0.077 (6)
C7	0.5786 (14)	0.7013 (11)	−0.0636 (10)	0.076 (6)
C6	0.7459 (14)	0.7773 (11)	−0.1608 (10)	0.079 (6)

constant (ε′) peak with $T_3 = \sim 289$ K, where peak's maximum decreases with increasing frequency. The observed temperatures of the dielectric constant anomalies are in reasonable agreement with DSC-transition temperatures.

Temperature dependence of the imaginary part of dielectric constant (ε") versus temperature is shown in Fig. 3b, where results similar to those of ε′-T are observed with split peak at nearly the same temperatures. Similar behavior is also noted for the low-temperature transition at $T_3 = 290 \pm 2$ K, but with smaller amplitude as seen in insert (ii). This indicates that peaks of (ε") correspond to the temperature at which the

Table 3
Anisotropic displacement parameters (Å)^2 of 7CoC.

7CoC	U_{11}	U_{12}	U_{13}	U_{22}	U_{23}	U_{33}
Co1	0.037 (6)	0.003 (5)	−0.007 (5)	0.052 (7)	−0.024 (5)	0.051 (6)
Cl2	0.048 (6)	0.005 (5)	−0.005 (5)	0.056 (7)	−0.023 (5)	0.050 (6)
Cl3	0.037 (6)	0.001 (5)	−0.008 (5)	0.056 (7)	−0.031 (5)	0.071 (6)
Cl4	0.043 (6)	0.004 (5)	−0.016 (5)	0.064 (7)	−0.018 (5)	0.060 (6)
Cl5	0.088 (6)	−0.003 (5)	−0.005 (5)	0.062 (7)	−0.040 (5)	0.065 (6)
N14	0.044 (6)	0.001 (5)	0.000 (5)	0.057 (7)	−0.021 (5)	0.051 (6)
C12	0.053 (6)	−0.005 (5)	0.007 (5)	0.061 (7)	−0.036 (5)	0.069 (6)
N13	0.066 (6)	0.003 (5)	0.007 (5)	0.054 (7)	−0.026 (5)	0.053 (6)
C11	0.055 (6)	0.002 (5)	−0.007 (5)	0.091 (7)	−0.023 (5)	0.055 (6)
C9	0.065 (6)	−0.013 (5)	0.001 (5)	0.098 (7)	−0.036 (5)	0.069 (6)
C10	0.057 (6)	−0.008 (5)	0.001 (5)	0.097 (7)	−0.019 (5)	0.054 (6)
C7	0.076 (6)	0.008 (5)	−0.010 (5)	0.082 (7)	−0.021 (5)	0.052 (6)
C6	0.071 (6)	−0.001 (5)	0.000 (5)	0.075 (7)	−0.033 (5)	0.073 (6)

Table 4
Selected bond distances, angles, dihedral angles and H-bond of 7CoC.

	7CoC	
Bond distances (Å)	Co1—Cl2	2.2871 (10)
	Co1—Cl3	2.2721 (9)
	Co1—Cl4	2.2837 (10)
	Co1—Cl5	2.2590 (11)
Bond angels (^{0})	Cl2—Co1—Cl3	111.48 (4)
	Cl2—Co1—Cl4	107.17 (4)
	Cl2—Co1—Cl5	110.83 (4)
	Cl3—Co1—Cl4	104.54 (4)
	Cl3—Co1—Cl5	108.94 (4)
	Cl4—Co1—Cl5	113.76 (4)
Dihedral angle (^{0})	C8—C7—C6—N13	66 (10)
	C6—C7—C8—C9	−179 (12)
	C7—C8—C9—C10	−175 (12)
	C8—C9—C10—C11	−179 (12)
	C9—C10—C11—C12	78 (10)
	C10—C11—C12—N14	−173 (12)
H. bond (Å)	Cl2—H13B	2.472 (2)
	Cl2—H14C	2.289 (2)
	Cl3—H14A	2.436 (2)
	Cl4—H13C	2.457 (2)
	Cl4—H14B	2.562 (2)

Table 5
Lattice potential energy (U_{pot}) (kJ/mol), molecular volume (V_m) (nm^3) and cation volume (V^+) (nm^3) of the hybrids 7CoC, 7CoCB and members of $[(CH_2)_n(NH_3)_2]CoCl_4$; n = 3, 5 and 6.

n	hybrid	U_{pot} kJ/mol	Vm nm^3	V^+ nm^3
3	3CoC	1986.6	0.272	0.076
5	5CoC	1927.2	0.314	0.118
6	6CoC	1886.5	0.349	0.153
7	7CoC	1856.2	0.378	0.182
7	7CoCB	1844.4	0.390	–
7	7CoB	1827.7	0.742	–

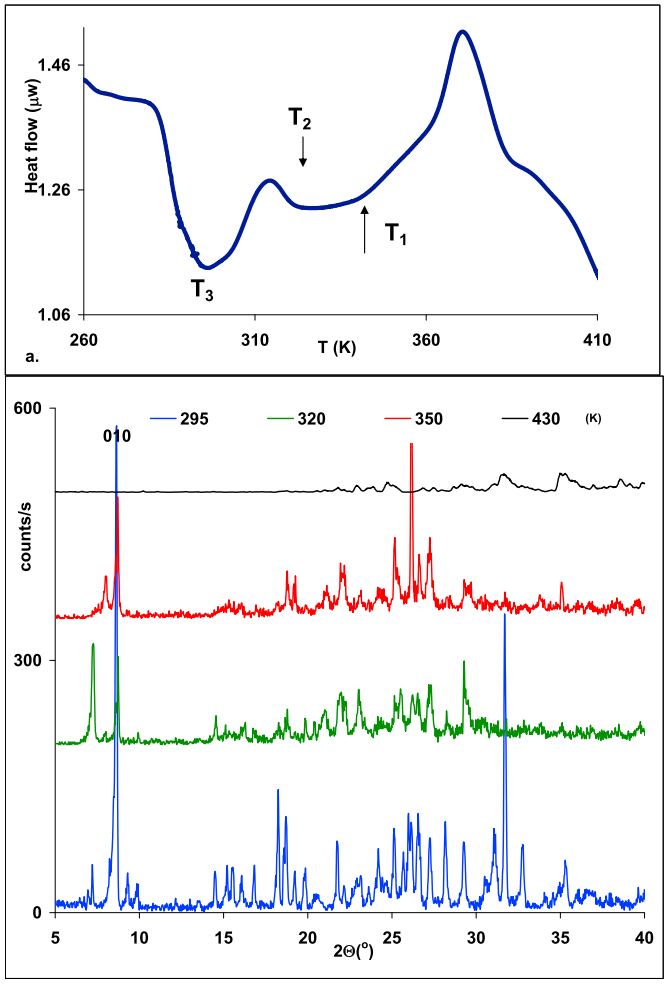

Fig. 2. a: DSC thermograph measured on heating between 260 K and 410 K.
Fig. 2. b: X-ray powder diffraction patterns at selected temperatures.

Table 6
Transition temperatures, enthalpy and entropy values of 7CoC.

Temperature range	T_3 (K)	T_2 (K)	T_1 (K)
heat 260- 360 K	296	328	331
ΔH (J/mol)	8251.86		10715.2
ΔS (J/K. mol)	24.9		36.2

dispersion of the real part attains maximum for all transitions.

3.4.2. ii. Frequency dependence of the dielectric constant

Frequency dependence of the real part of dielectric constant on logarithmic plot [ln (ε′)-ln (ω/ω0)] at selected temperatures is shown in Fig. 4a. The graph shows nearly linear dependence given by $\varepsilon' \alpha\ \omega^{-n1}$. Fig. 4b depicts variation of the slope $n_1 = d\ [\ln (\varepsilon')]/d\ [\ln (\omega/\omega_0)]$ with temperature in the linear region. It is found that n shows two sharp minima at 326 K and 331 K in excellent agreement with DSC transitions. Another shallow, less pronounced minimum is observed at T = ~287 K as seen in insert (i), which corresponds to transition T_3.

Fig. 4c depicts the frequency dependence of the imaginary part of dielectric constant as [ln (ε")] vs. [ln (ω/ω0)]. For frequencies f < 10 kHz and at high temperatures, linear dependence of ε" is observed according to $\varepsilon'' \alpha \omega^{-n2}$. The graph is characterized by a shallow minimum that shifts to higher frequencies with increasing temperature. This implies change from universal dielectric relaxation (UDR) [49] to the super-linear power law (SLPL) [50] as suggested by Lunkenheimer and Loidl [51,52].

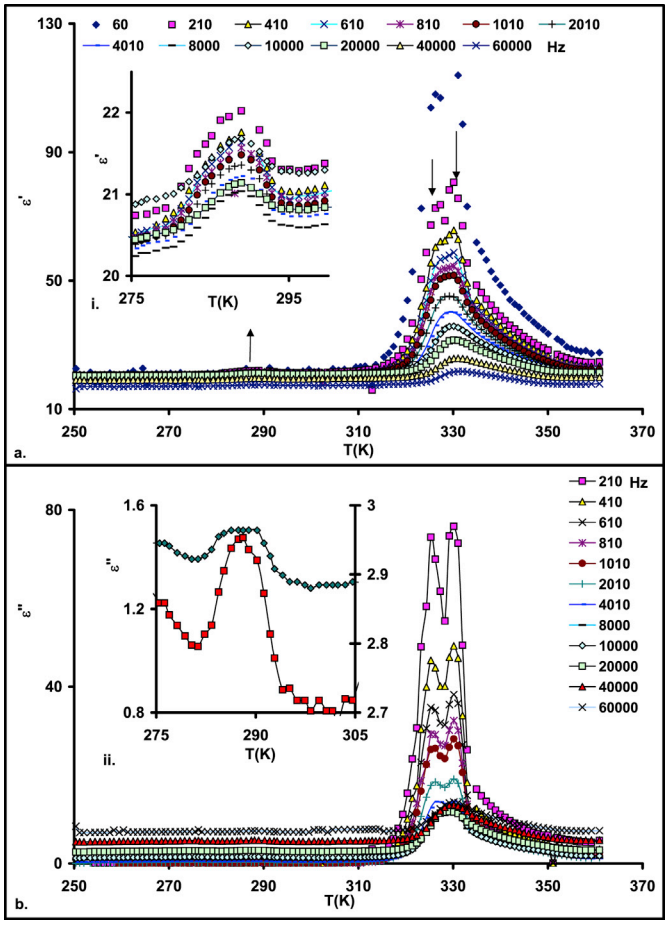

Fig. 3. a: Real part (ε′) of dielectric constant vs. temperature between 260 K and 360 K. Insert (i): Real part (ε′) of dielectric constant vs. temperature between 275 K and 300 K.
Fig. 3. b: Imaginary part (ε′) of dielectric constant vs. temperature between 260 K and 360 K. Insert (ii): Imaginary part (ε′) of dielectric constant vs. temperature between 275 K and 305 K.

3.5. Conductivity results

3.5.1. i Temperature dependence

Fig. 5 a shows temperature dependence of AC conductivity [ln (σ_{AC})] vs. 1000/T (K) at selected frequencies. Conductivity is temperature and frequency dependent, with all curves tending to merge at the transition temperature $T_1 = 331$ K. A change in slope of [ln (σ_{AC})] vs. 1000/T (K) can be due to phase transitions or reflect a change in conduction mechanism. For the presently investigated sample, observed changes in the conductivity can be attributed to the phase transition that could be associated with changes of conduction mechanism. The graph shows two regions, where conductivity is thermally activated. A high-temperature region (315 K–323 K) and a low-temperature region (T < 274 K) identified as phases I and II, respectively, where Arrhenius relation holds. Regions denoted IT refers to the intermediate range where phase transitions take place and Arrhenius relation could not be used. At low temperatures, T < 274 K (phase II), data scattering for f < 1.0 kHz is observed; however, activation energy values were obtained within acceptable error margin at higher frequencies. Low activation energy values ΔE = 0.35 eV–0.013 eV fit well with exponential decay with frequency. In phase I, activation energy (ΔE) is frequency dependent according to Eq. (7)

$$\Delta E = \Delta E_0\ [1\text{-}\exp\ (-f_0/f)]^{\ \alpha} \qquad (7)$$

where ΔE_0 is the activation energy in the limit f → 0 and α is a constant

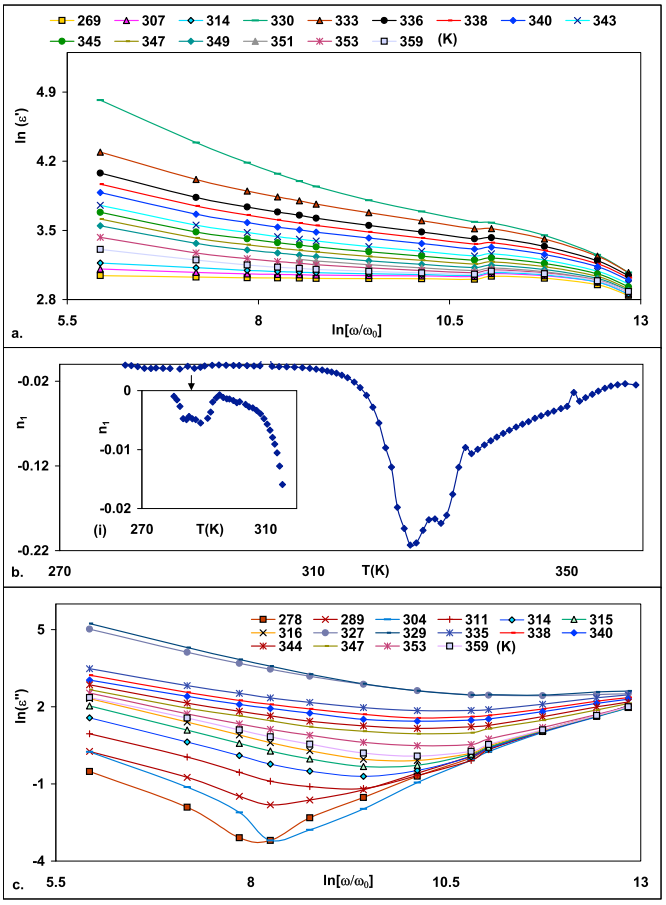

Fig. 4. a: Real part [ln (ε′)] of dielectric constant vs. angular frequency [ln (ω/ω0)] at selected temperatures between 269 K and 359 K ω0 is a reference value, taken to be 1 s–1.
Fig. 4. b: Slope n1 = d [ln (ε′)]/d [ln (ω/ω0)] vs. T (K).
Fig. 4. c: Imaginary part [ln (ε′)] of dielectric constant vs. angular frequency [ln (ω/ω0)] at selected temperatures between 269 K and 360 K.

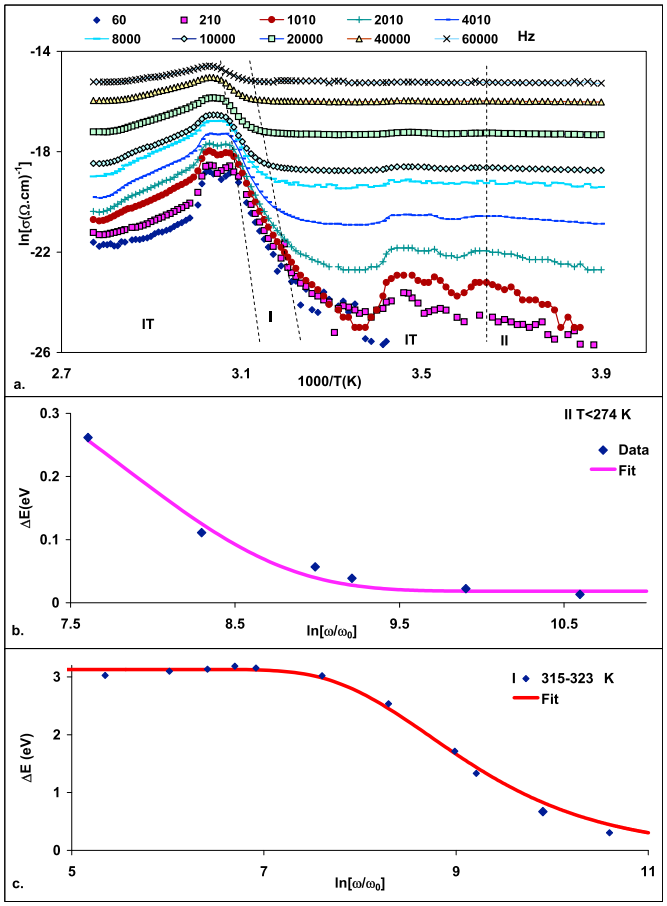

Fig. 5. a: AC conductivity [ln (σAC)] vs. 1000/T (K) at selected frequencies [f (Hz)].
Fig. 5. b: Activation energy ΔE vs. [ln (ω/ω0)] of 7CoC and fit in phase II.
Fig. 5. c: Activation energy ΔE vs. [ln (ω/ω0)] of 7CoC and fit in phase I.

with values between 0 and 1.0.

The results of the fit are displayed as a function of [ln (ω/ω0)], as depicted in Fig. 5b and 5 c. Fit parameters are listed in Table 7. Lines are the fit and symbols are data points. The high ΔE values could be attributed to the fact that the temperature range where ΔE is calculated (315–323 K) is near the boundary of the phase transition range where several species are responsible for conduction (e.g., Cl ion hopping among vacant sites [53], proton hopping as well as librational motion of the organic chain). Considering the structural characteristics of the sample, conduction is related to movement of the ammonium group and its relation to the hydrogen bonding with the chloride ion. It is likely that in the neighborhood of the chain melting transition, as the hydrogen bond breaks, simultaneous jump of both chloride ions and protons among vacant sites takes place. In addition, as the N–H···Cl bonds weakens, correlated orientation of the organic chains is facilitated, which will contribute to the activation energy.

3.5.2. ii Frequency dependence

It is found that the AC conductivity increases with increase of angular frequency, revealing that bound carriers are trapped in the sample. The dependence of conductivity σ_{AC} on temperature and frequency (ω,T) may be divided into two regions. A low-temperature, low-frequency range ($T < 311$ K, $\ln\omega < 8.25$), where σ_{AC} is nearly frequency independent, and a high-temperature, high-frequency range ($T > 311$ K, $\ln\omega > 8.25$), where σ_{AC} is frequency dependent such that its dependence on frequency decreases as temperature rises. According to Jonscher's universal dispersion relaxation (UDR) [49], electric conduction is a thermally activated process and the origin of frequency dependence of conductivity is related to the relaxation phenomena due to mobile charge carriers. It can be expressed by the relation

$$\sigma_{AC} = \sigma_{DC} + A\omega^{s} \quad (8)$$

where σ_{AC} and σ_{DC} are the AC and DC conductivity, respectively; A and s are temperature-dependent fitting parameters ($0 \le s \le 1$) and ω is the angular frequency.

The fit of σ_{AC} to Eq. (8) was not successful. Reasonably good fits were obtained using SLPL as given by Eq. (9) [50,54]:

$$\sigma_{AC} = \sigma_{DC} + A_1\omega^{s1} + A_2\omega^{s2} \quad (9)$$

Fig. 6 a shows data of AC conductivity [ln (σ_{AC})] with angular frequency [ln (ω/ω0)]. AC conductivity σ_{AC} increases with increase of angular frequency. Fig. 6 b displays fit of [ln (σ_{AC})] vs. [ln (ω/ω0)] to Eq. (9) at selected temperatures. σ_{DC}, as obtained from fit to Eq. (9), is plotted in Fig. 6 c as [ln (σ_{AC})] vs. 1000/T (K). The calculated activation energy

Table 7
Activation energy and its fit parameters to Eq. (7) of 7CoC.

Phase	T(K)	ΔE (eV)	E_0 (eV)	F_0 (Hz)	α
I	315–323	3.08–0.18 (0.60–60 kHz)	3.13 ± 0.03	5918 ± 290	1.0 ± 0.0
II	T < 274	0.45–0.013 (2.01–40 kHz)	exp. decay ΔE = 1.70*exp (-f/1449) +0.031		

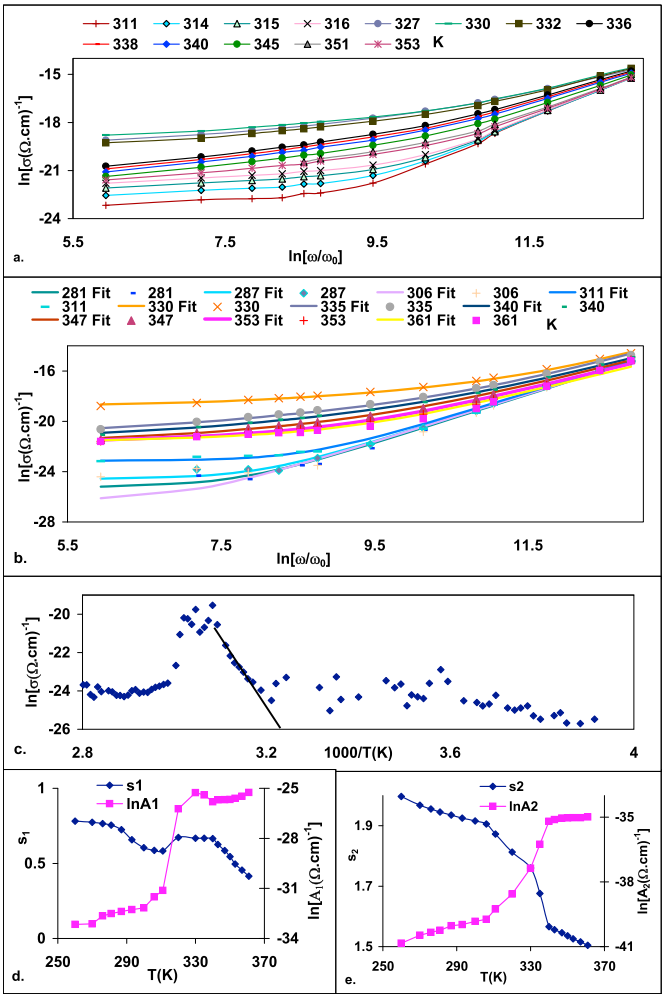

Fig. 6. a: Experimental results of [ln (σAC)] vs. [ln (ω/ω0)].
Figs. 6. b: Fitted data of [ln (σAC)] vs. [ln (ω/ω0)] according to Eq. (9). Lines represent fits; symbols represent data.
Fig. 6. c: Results of [ln (σDC)] vs. 1000/T (K) as obtained from fit to Eq. (9).
Fig. 6. d Fitting parameters s1 and [ln (A1)] vs. T (K) as obtained from fit to Eq. (9).
Fig. 6. e: Fitting parameters s2 and [ln (A2)] vs. T (K) as obtained from fit to Eq. (9).

in the temperature range 315 K–321 K yields a value of $\Delta E = 3.23$ eV, which is very close to that obtained using Eq. (7), further confirming the goodness of fit. Fig. 6 d and 6. e displays the variations of the fit parameters s_1 [ln (A_1)] and s_2 [ln (A_2)] with temperature. The graphs reflect anomalous changes at the observed phase transitions. The general trend of decreasing s_1 and s_2 with increasing temperature could reasonably be associated with correlated barrier hopping [55].

Crystal structure analysis of $[(CH_2)_n (NH_3)_2]CoCl_4$, n = 3, 5, 6, and 7 indicated that short-chain hybrids (n = 3 and 5) crystallize in monoclinic structure as observed in hybrids having different metal ions (Mn, Fe, Cu, and Cd), whereas long-chain hybrids (n = 6 and 7) are triclinic. Comparison of structural differences between short- and long-chain hybrids reveals that long-chain hybrids are characterized by weaker hydrogen bonding and more distorted $[CoCl_4]^{2-}$ tetrahedra. Besides, the dihedral angles of 3CoC and 5CoC are nearly constant, varying within 4° and 3°, respectively. Long-chain length hybrids showed dihedral angles in the range 179 (all *trans*) except near the terminal ends C9–C10–C11–C12 and C8–C7–C6–N13, where the dihedral angles are approximately –61°, 71° and approximately –67° and 79.3° for 6CoC and 7CoC, respectively. Chain length with *trans* conformation crystallizes in the triclinic system, but not in the high-symmetry monoclinic system to attain the most stable conformation.

Regarding the thermal properties of $[(CH_2)_n (NH_3)_2]CoCl_4$, the only available results below melting are those for 6 and 12. Several consecutive endothermic peaks were revealed for 6CoC where four transitions at $T_1 = 404$ K, $T_2 = 330$, $T_3 = 317$, and $T_4 = 197$ K [20] were observed and five transitions at $T_1 = 396$ K, $T_2 = 337$ K, $T_3 = 316$ K, $T_4 = 288$, and $T_5 = 188$ K were observed for 12CoC [30]. Endothermic peaks at T_2 and T_3 were attributed to conformational changes in the polymethylene chains and rotation of the chain around its own axis. Comparison of 6CoC ($T_2 = 330$ K), 7CoC ($T_1 = 331$ K), and 12CoC ($T_2 = 337$ K) shows a shift to higher temperature as the chain length increases. It is also noted that transition temperature T_2 of 7CoCB (333.8 K) and 7CoB (335 K) is shifted to higher temperatures in comparison to T_1 of 7CoC (331 K), see Table 6. Thus a shift of transition temperatures is noted by increasing the chain length and bromide ion. It is important to point to the fact that different temperatures of transitions associated with dielectric and conductivity anomalies of hybrids containing different halide ions reflect structural transitions that are not only due to the organic chain, but must also be influenced by the tetrahedral $[CoX_4]^{2-}$ anion, X = Cl/Br. X-ray structure data show an increase of bond distances from $r_{(M-X)} = 2.27 \pm 0.02$ Å to 2.36 ± 0.05 Å to 2.41 ± 0.01 Å for 7CoC, 7CoCB, and 7CoB, respectively. Besides, the conformation and rotational motion of $[(CH_2)_7(NH_3)_2]^{2+}$ and the rotation of the $[CoX_4]^{2-}$ tetrahedron along an axis passing through the Co ion occur. As the heavier bromide ion replaces chloride, the size, mass, and moment of inertia of the tetrahedron increase. Hence energies of the soft modes involved in the phase transition sequence shift accordingly [56], which would account for the observed shift of the transition temperatures.

It is interesting to relate the effect of changing halide ions on conductivity behavior. Activation energy values, within nearly the same temperature range, were found to be $\Delta E_0 = 3.13 \pm 0.03$ eV, 1.9 ± 0.04 eV, and 0.66 ± 0.02 eV for 7CoC, 7CoCB, and 7CoB, respectively, and their frequency dependence are listed in Table 7. It is clear that the activation energy decreases as the bromide ion increase. This is not surprising because as bromide increases, the tetrahedron size will increase. Thus the ratio of the $[CoX_4]^{2-}$ size to that of $[(CH_2)_7(NH_3)_2]^{2+}$ will increase. Therefore the available space for $[CoX_4]^{2-}$ will be larger. It is expected that the change in the available space will affect the organic chain motion as well. Hence it will influence the mobility of the conducting species, Cl^-, Br^-, and hydrogen, associated with N–H … X bonding, as well as the librational motion of the chain. The N–H … X bond length is 2.443 Å, 2.595 Å, and 2.745 Å for 7CoC, 7CoCB, and 7CoB, respectively, indicating weaker bonds in bromide hybrids and thus lower activation energy.

4. Conclusion

$[(CH_2)_7(NH_3)_2]CoCl_4$ crystallizes in triclinic systems (P-1). It consists of alternating layers of inorganic $[CoCl_4]^{2-}$ anion hydrogen bonded to heptane diammonium cation and is isomorphous to other previously studied members of long-chain hybrids, namely, 6CoCl, 7CoCB, and 7CoB. Its structure is different from the short-chain hybrids (3CoC and 5CoC) that crystallized in monoclinic systems. It undergoes three phase changes at $T_1 = 331$ K, $T_2 = 328$ K with total entropy $\Delta S = 36.2$ J/K mol and $T_3 = 296$ K ($\Delta S = 24.9$ J/K. mol). T_1 and T_2 are associated with chain melting transition that involves conformations and rotation of the organic chain. The large entropy value suggests order–disorder transition. Chain melting transitions are also observed in the temperature range 316–335 K for 6CoCl, 7CoCB, and 7CoB. Transition temperatures shift to higher values upon replacing Cl^- by Br^-. 7CoC shows maxima in the dielectric constant, reflecting the structure transformation. A similar trend of increase in the transition temperature is observed when comparing 6CoC, 7CoC, and 12CoC. The calculated lattice potential energy indicated a decrease as the chain length increases and as the inorganic ion size increases. Conductivity of 7CoC, 7CoCB, and 7CoB hybrids is thermally activated with different activation energy depending on the

temperature range. Replacement of chloride by bromide results in a decrease of the activation energy related to differences in size, mass, and moment of inertia of the cobalt halide tetrahedra. Conduction takes place via halide ion and proton hopping as well as via the librational motion of the organic chain. Conduction mechanism is the same for the three hybrids, irrespective of the halide ion, where super-linear power law prevails.

Acknowledgments

The authors acknowledge Professor E.M. Kandeel of Mansoura University for the discussion and critical reading of the manuscript.

References

[1] C. Sanchez, P. Belleville, M. Popall, L. Nicole, Chem. Soc. Rev. 40 (2011) 696–753.
[2] P. Li, W. Liao, Y. Tang, H. Ye, Yi Zhang, R. Xiong, J. Am. Chem. Soc. 139 (2017) 8752–8757.
[3] F. Zheng, D. Saldana-Greco, S. Liu, A. Rappe, J. Phys. Chem. Lett. 6 (2015) 4862–4872.
[4] Y. Zhao, K. Zhu, Chem. Soc. Rev. 45 (2016) 655–689.
[5] L.J. De Jongh, A.R. Miedema, Adv. Phys. 50 (2001) 947–1170.
[6] R. Kind, S. Plesko, P. Gunter, J. Roos, J. Fousek, J. Phys. Rev. B23 (1981) 5301–5315.
[7] M. Maczka, A. Pietraszko, B. Macalik, K. Hermanowicz, Adv. Funct. Mater. 7 (2017) 1603945–1603953, https://doi.org/10.1021/ic4020702.
[8] S. Slomkowski, Polimery-Warsaw 51 (2006) 87–94.
[9] Y.W. Wang, C.T. Yen, W.C. Chen, Polymer 46 (2005) 6959–6967.
[10] R.D. Willett, E.F. Riedel, Chem. Phys. 8 (1975) 112–122.
[11] J. Garland, K. Emerson, M. Pressprich, Acta Cryst C46 (1990) 1603–1609.
[12] A. Lamhamdi, E. Mejdoubi, K. Fejfarova, M. Dusek, B. El Bali, Acta Cryst E65 (2009) m215–216.
[13] M. Khechoubi, A. Bendani, N. Chanh, C. Courseille, R. Duplessix, M. Couzi, J. Phys. Chem. Sol 55 (1994) 1277–1288.
[14] P. Negrier, N. Chanh, C. Courseille, C. Hauw, A. Meresse, M. Couzi, Phys. Stat. Sol. 100 (1987) 473–483.
[15] H. Arend, K. Tichy, K. baberschke, F. Rys, Sol. Stat. Comm 18 (1976) 999–1003.
[16] G. Ning, L. Young-Hua, Z. Guang-Fu, X. Shi-Quan, Acta Cryst. C48 (1992) 542–543.
[17] A. Kallel, J. Fail, H. Fuess, A. Daoud, Acta Cryst B36 (1980) 2788–2790.
[18] J. Criado, A. Jiménez-Sánchez, F.H. Cano, R. Sáez-Puche, E. Rodríguez-Fernández, Acta Cryst. B55 (1999) 947–952.
[19] A.H. Mahmoudkhani, V. Langer Acta Cryst., E 58 (2002) m592–m594.
[20] S. Sh, Ph Khiyami, D. Physics Department, University of Cairo, Egypt, 2012.
[21] M.F. Mostafa, S.S. El-khiyami, J. Sol. Stat. Chem. 209 (2014) 82–88.
[22] M.F. Mostafa, S. Abd-elal, A.K. Tammam, Indian J. Phys. 88 (2014) 49–57.
[23] M.F. Mostafa, S.S. ElKhiyami, S.A. Alal, Mat. Chem. Phys. 199 (2017) 454–463.
[24] www.ccdc.cam.ac.uk/data request/cif CCDC 1437813.
[25] K. Elmebrouki, S. Tamsamani, M. Khechoubi, J. Asian, Sci. Res. 1 (2011) 216–219.
[26] M.A. Ahmed, M.F. Mostafa, M. Mohamed, Phys. Stat. Sol.(a) 69 (1982) K103–K108.
[27] M.F. Mostafa, M. AbdelKader, S. Arafat, Z. Naturforsch. 57a (2002) 897–908.
[28] M.F. MostafaA, A. Youssef, Z. Naturforsch. 59a (2004) 35–46.
[29] M.F. MostafaA, A. Youssef, Z. Naturforsch. 56a (2001) 568–578.
[30] M.F. Mostafa, A.A. Youssef, S.S. El- Hakim, Phase Transitions 77 (2004) 317–333.
[31] M.F. Mostafa, A.A. Youssef, S.A. El- Hakim, Phase Transitions 76 (2003) 587–599.
[32] M.F. Mostafa, Arafa Hassen, Phase Transitions 79 (2006) 305–321.
[33] R. L, Carlin Magnetochemistry, Springer Verlag, New York, 1986, p. 19.
[34] R.L. Carlin, Science 227 (1985) 1291–1295.
[35] F. Sanz, C. Valero, J. Rojo, C. Parada, R. Puche, J. Solid State Chem. 145 (1999) 604–611.
[36] Z. Otwinowski, W. Minor, in: C.W. Carter Jr., R.M. Sweet (Eds.), Processing of X-ray Diffraction Data Collected in Oscillation Mode. Macromolecular Crystallography Part a, Academic Press, NY, 1997.
[37] A. Altomare, G. Cascarano, C. Giacovazzo, A. Guagliardi, M.C. Burla, G. Polidori, M. Camalli, J. Appl. Cryst 27 (1994) 435.
[38] S. Mackay, C.J. Gilmore, C. Edwards, N. Stewart, K. Shankland, *maXus* Computer Program for the Solution and Refinement of Crystal Structures Bruker Nonius The Netherlands MacScience Japan and the University of Glasgow, 1999.
[39] C.K. Johnson, ORTEP—ii a Fortran Thermal–Ellipsoid Plot Program Report ORNL-5138, Oak Ridge National laboratory, Oak Ridge Tennessee USA, 1976.
[40] www.ccdc.cam.ac.uk/data_request/cif.
[41] G. Ning, Z. Guangfu, X. Shiquan, J. Phys. Chem, Sol 53 (1992) 437–441.
[42] L. Glasser, H.D.B. Jenkins, Inorg. Chem. 47 (2008) 6195–6202.
[43] H.D.B. Jenkins, L. Glasser, Inorg. Chem. 41 (2002) 4378–4388.
[44] W. Li, D. Zhang, T. Zhang, T. Wang, D. Ruan, D. Xing, H. Li, Thermochim. Acta 326 (1999) 183–186.
[45] R. Parashkov, Progress in Advanced materials Research, in: N.H. Voler (Ed.), Nova Science Publishers, New York, 2007 (Chapter 4).
[46] H. Abid, A. Trigui, A. Mlayah, E.K. Hlil, Y. Abid, Results in Phys. 2 (2012) 71–76.
[47] J. Aazza, K. Elmebrouki, M. Khechoubi, A. Khmou, J. Asian Scientific Research. 3 (2013) 1072–1077.
[48] R. Kind, S. Plesko, J. Roos, Phys. Stat.Sol (a). 47 (1978) 233–240.
[49] A.K. Jonscher, Dielectric Relaxation in Solids. Publisher, Chelsea Dielectric Press, London, 1983.
[50] P. Extance, S. Elliott, E. Davis, J. Phys. Rev B. 32 (1985) 8148–8161.
[51] P. Lukenheimer, A. Loidl, Broadband dielectric Spectroscopy, in: F. Kremer (Ed.), Schonhals, Springer-Verlag, Berlin, 2002. P.131.
[52] P. Lunkenheimer, A. Loidl, Phys. Rev. Lett. 91 (2003), 207601-(4).
[53] J.F. Scott, Rep. Prog. Phys. 42 (1979) 1055–1084.
[54] M. Le, Stanguennec, S.R. Elliott, Sol. Stat. Ionics. 73 (1994) 199–208.
[55] S.R. Elliott, Sol. Stat. Ionics. 70/71 (1994) 27–40.
[56] G. Venkataraman, Bull. Mater. Sci. 1 (1979) 129–170.